

Pushing the boundaries
of chemistry?
It takes
#HumanChemistry

Make your curiosity and talent as a chemist matter to the world with a specialty chemicals leader. Together, we combine cutting-edge science with engineering expertise to create solutions that answer real-world problems. Find out how our approach to technology creates more opportunities for growth, and see what chemistry can do for you at:

[evonik.com/career](https://www.evonik.com/career)



Gas-Phase Fluorination of Hexagonal Boron Nitride

AshokKumar Meiyazhagan,* Peter Serles, Devashish Salpekar, Eliezer Fernando Oliveira, Lawrence B. Alemany, Riqiang Fu, Guanhui Gao, Taib Arif, Robert Vajtai, Venkataraman Swaminathan, Douglas S. Galvao, Valery N. Khabashesku,* Tobin Filleter,* and Pulickel M. Ajayan*

Hexagonal boron nitride (*h*BN) has received much attention in recent years as a 2D dielectric material with potential applications ranging from catalysts to electronics. *h*BN is a stable covalent compound with a planar hexagonal lattice and is relatively unreactive to most chemical environments, making the chemical functionalization of *h*BN challenging. Here, a simple, scalable strategy to fluorinate *h*BN using a direct gas-phase fluorination technique is reported. The nature of fluorine bonding to the *h*BN lattice and their chemical coordination are described based on various characterization studies and theoretical models. The fluorine functionalized *h*BN shows a bandgap reduction and displays a semiconducting behavior due to the fluorination process. Additionally, the fluorinated *h*BN shows significant improvement in its thermal and friction properties, which could be substantial in applications such as lubricants and thermal fluids. Theory and simulations reveal that the enhanced friction properties of fluorinated *h*BN result from reduced interplanar interaction energy by electrostatic repulsion of intercalated fluorine atoms between *h*BN layers without significant disruption of the in-plane lattice. This technique paves the way for the fluorination of several other 2D structures for various applications such as magnetism and functional nanoscale electronic devices.

properties and their wide range of potential applications in several fields.^[1–6] As a result, many different 2D materials have been functionalized to enhance and tune their physical and electronic properties. Among them, hexagonal boron nitride (*h*BN), commonly referred to as “white graphene,” has been critically studied as a 2D material due to its promising applications, including electronics, energy storage, catalysis, lubricants, and composite reinforcement.^[7,8] *h*BN shows a hexagonal atomic arrangement analogous to that of graphite in which alternating boron (B) and nitrogen (N) atoms form an interlocking hexagonal ring connected through strong covalent sp^2 hybridized B–N bonds formed between sp^2 hybridized B and N atoms. *h*BN behaves as a typical electrical insulator; however, a few theoretical calculations^[9,10] and experimental studies^[4,11] have demonstrated bandgap reduction due to effective chemical functionalization yielding n-type semiconductor behavior.^[4] On the other hand, the interplanar B–N


layers are stacked together with weak van der Waals forces, which help to provide incommensurate contacts leading to the strong lubrication performance characteristic of van der Waals materials.^[12] Hence, *h*BN is used as an additive in many

1. Introduction

Functionalization of various 2D structures has gained prime interest in recent decades due to their unique, fascinating

A. Meiyazhagan, D. Salpekar, E. F. Oliveira, G. Gao, R. Vajtai, V. Swaminathan, V. N. Khabashesku, P. M. Ajayan
Department of Materials Science & NanoEngineering
Rice University
Houston, TX 77005, USA
E-mail: ma37@rice.edu; khval@rice.edu; ajayan@rice.edu
P. Serles, T. Arif, T. Filleter
Department of Mechanical & Industrial Engineering
The University of Toronto
5 King's College Road, Toronto, Ontario M5S 3G8, Canada
E-mail: filleter@mie.utoronto.ca
E. F. Oliveira, D. S. Galvao
Group of Organic Solids and New Materials
Gleb Wataghin Institute of Physics
University of Campinas (UNICAMP)
Campinas, São Paulo 13.083-861, Brazil

E. F. Oliveira, D. S. Galvao
Center for Computational Engineering and Sciences (CCES)
University of Campinas (UNICAMP)
Campinas, São Paulo 13.083-861, Brazil
L. B. Alemany
Shared Equipment Authority
Rice University
Houston, TX 77005, USA
L. B. Alemany
Department of Chemistry
Rice University
Houston, TX 77005, USA
R. Fu
National High Magnetic Field Laboratory
1800 E. Paul Dirac Drive, Tallahassee, FL 32310, USA

 The ORCID identification number(s) for the author(s) of this article can be found under <https://doi.org/10.1002/adma.202106084>.

DOI: 10.1002/adma.202106084

such lubrication applications.^[13,14] However, in general, the strong chemical stability and the compact packing of BN layers increase the shear modulus, which reduces its effectiveness as a lubricant.^[15] As a result, it is essential to effectively functionalize BN with heteroatoms, which can intercalate to reduce the interplanar van der Waals potential and improve lubricity and mechanical performance.

Various strategies have been reported towards functionalization or doping of *h*BN, including heteroatom substitution, stannic oxide coating, and functionalization or intercalation of hydroxy,^[16–19] amino,^[20–22] alkyl,^[23] and halogen groups.^[24,25] Similarly, several theoretical studies have suggested the possibility of fluorination of the boron nitride systems and their significance.^[26,27] It is well known that fluorine (F), the lightest halogen and the most reactive one with the highest electronegativity, possesses excess valence electrons compared to B and N atoms. Therefore, the fluorination process of BN structures is expected to change the electronic, optical, and magnetic properties significantly.^[23,26] However, the practical feasibility of the fluorination of BN has been thus far limited. Moreover, fluorination chemistry, the resulting chemical structure, and properties of these fluorinated structures remain unexplored and hence are of much interest. While some previous reports suggest the possibility of fluorination of BN using sources such as Nafion^[11] or ammonium fluoride^[28] using hydrothermal techniques, these methods still pose significant limitations such as selectivity, repeatability, scalability, by-product formation, extended (>24 h) reaction time, and comprehensive washing process using several hazardous solvents.

To overcome these complexities, we demonstrate a straightforward chemical and solvent-free approach to produce fluorinated hexagonal boron nitride (F-*h*BN) and study their chemistries, bandgap reduction, and their resulting semiconducting behavior. Additionally, we used several techniques to understand the chemical environment, nature, and thermal stability of the formed F-*h*BN bonds and studied the friction behavior since BN is considered a strong lubricant under different environmental conditions.

2. Results and Discussion

Figure 1a displays the fluorination process' schematic, and the possible atomic arrangement of fluorine in F-*h*BN is shown in Figure 1b. The detailed protocol of fluorination is described in the methods section. In brief, the fluorination process was carried out at two different conditions of room temperature (RT) and 50 °C for 1 and 2-h durations by passing a mixture of fluorine (F₂)/Helium (He) gas to the BN powder placed in a Teflon boat.

The real-time photographs of *h*BN and F-*h*BN powders are shown in Figure S1, Supporting Information. The interaction of highly electronegative fluorine atoms with the BN results in B-F and N-F bond formation as confirmed using several analytical techniques. The Fourier Transform Infrared Spectroscopy (FTIR) spectra of pristine *h*BN and F-*h*BN derived at different conditions are shown in Figures 1c and Figure S2, Supporting Information. The pristine *h*BN shows two predominant peaks around 779 and 1363 cm⁻¹. The sharp vibrational peak centered

around 779 cm⁻¹ is characteristic of the out of the plane (A_{2u} mode), and the broader peak at ≈1363 cm⁻¹ resembles the in-plane vibrations (E_{1u} mode) of the *h*BN, which matches with the previous reports.^[29] The F-*h*BN samples displayed new peaks at ≈523 cm⁻¹, between 1020–1070 cm⁻¹, and 3200 cm⁻¹ (Figure 1c and Figure S2, Supporting Information), which correspond to the newly formed N-F and B-F bands;^[30,31] the predominant peaks around 1020–1070 and 3200 cm⁻¹ correspond to the presence of covalent B-F bonds,^[4,31,28] and the weak signals at 523 cm⁻¹ were assigned to the asymmetric N-F bending vibrations.^[32–34]

High-resolution XPS analysis was carried out to understand the nature and coordination of fluorine bonding with the boron and nitrogen atoms. The results of fluorinated *h*BN samples under various conditions show the presence of B, N, and F atoms (Figure 1d–f and Figures S3–S6, Supporting Information). The atomic percentage (at%) of the fluorine changes with respect to changes in temperature, duration of fluorination (Figure S7, Supporting Information), and the particle size of *h*BN (Table S1, Supporting Information). The detailed XPS analysis of *h*BN fluorinated at 50 °C for a 2h duration is shown in Figure 1d–f, and the corresponding survey scan is depicted in Figure S6, Supporting Information. The deconvoluted high-resolution B1s spectra reveal the presence of three distinct chemical bonding states (Figure 1d). The first peak observed around 190.2 eV corresponds to the B-N bond in *h*BN,^[11,29,35] and the second and third peak noticed around 191.3 and 193.4 eV were assigned to the origin of covalent B-F bonds and BF₂ structures respectively.

The deconvoluted N(1s) spectra (Figure 1e) display -N-B-bonding around 398.2 eV, assigned to the N-F bond formation.^[29,36,37] In general, direct addition of fluorine at the nitrogen site or stable N-F bond formation are not feasible due to both the elements' high electronegative nature. The mechanism of N-F bond formation can be explained with two possibilities: i) the formation of a stable B-F creates a partial positive charge on the adjacent nitrogen atom, which can directly form a bond with fluorine, or ii) addition of two fluorine atoms at the boron site and migration of one of the fluorine atoms to the adjacent nitrogen atom. In either of these cases, a geometry with (F)B-N(F) can be observed. Further, the fluorination may give rise to other possible substructures such as B(F₂)-N, -N(F)-B(F₂), etc., as discussed in DFT but, these substructures are trivial, and unstable.

The deconvoluted fluorine F(1s) spectra displayed two bands, one at 686.3 eV (≈80.6 at%) and another around 683.5 eV (19.4 at%), which can be assigned to the formation and relative abundance of the more stable covalent B-F and a weaker N-F bonds respectively.^[28,38] Another important observation is the increase in F concentration of F-*h*BN derived at 50 °C, which correspondingly displays an increase in FTIR intensity of 1034 cm⁻¹ peak (Figure 1c and Figure S2, Supporting Information), suggesting that the B-F bond is favored over the N-F bond. This correlation explains why the peak at 523 cm⁻¹ (attributed to N-F vibrations) is not obviously seen in the samples fluorinated at 50 °C. These observed XPS results correlate well with the FTIR observation.

Scanning transmission electron microscopy (STEM) images of the derived F-*h*BN were acquired by double corrector Titan

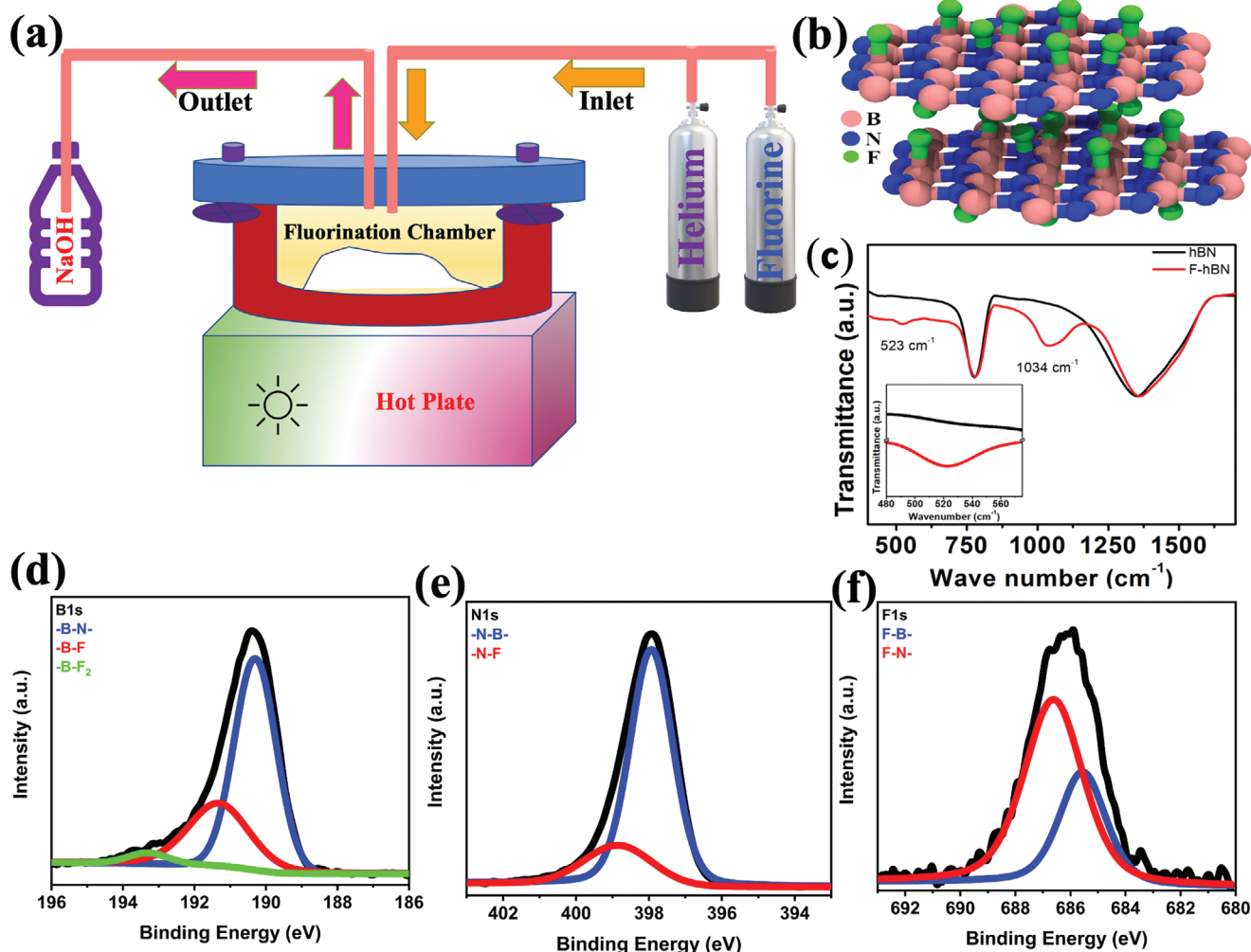


Figure 1. a) Schematic showing the fluorination chamber and the experimental setup. The fluorination chamber was connected with inflow fluorine, helium gas, and an outlet scrubber filled with sodium hydroxide (NaOH) to trap residual fluorine gas. b) The possible atomic configuration of fluorine in the F-hBN. c) FTIR spectra of the pristine hBN powder and the sample fluorinated at 50 °C for 2 h duration, which displays emergence of a new peak at 1034 and 523 cm^{-1} , which correspond to the newly formed B-F and N-F bonds. (The inset shows the N-F peak around 523 cm^{-1}). d–f) shows deconvoluted high-resolution X-ray photoelectron spectroscopy (XPS) analysis of hBN samples fluorinated at 50 °C for 2 h and their corresponding d) B1s, e) N1s, f) F1s spectra.

STEM, and the results are shown in Figure 2a and Figure S8, Supporting Information. The low magnification microscopic image displayed in Figure 2a shows the presence of several transparent, ultrathin functionalized hBN stacked into a few-layer sheet. The functionalized hBN sheets are highly crystalline, confirming that the fluorination process did not damage the derived F-hBN sheets. Higher magnification images (Figure S8a,b, Supporting Information) demonstrate the presence of several stacked functionalized BN sheets with interesting Moiré patterns (Figure S8b, Supporting Information), which resulted from the restacking of the hBN layers during the fluorination process. The high-angle annular dark-field (HAADF-STEM) mapping shows F, B, and N atoms (Figure S9, Supporting Information). The detailed mappings confirm the even distribution of all elements, as shown in Figure 2b–d, respectively. The SAED pattern shows six-fold symmetry, a typical feature of hBN (Figure 2a inset). Additionally, we carried out electron

energy loss spectroscopy (EELS) and STEM EDS to confirm the presence of specific elements. These techniques are more precise to evaluate the presence of lighter and sensitive elements like fluorine, and the corresponding results are shown in Figures S10 and S11, Supporting Information, respectively. The scanning electron microscopy (SEM) studies were carried out on F-hBN to understand the effect of fluorination (Figure S12, Supporting Information). Interestingly, no reasonable surface modification was seen on fluorinated hBN's. Figure S13, Supporting Information shows the stacking of few-layered BN sheets, and their corresponding SEM-EDX result (Figure S14, Supporting Information) displays Fluorine's presence in the derived F-hBN. The observed results correlate well with FTIR and XPS studies.

We further performed nuclear magnetic resonance (NMR) studies to understand the chemical environment of F-hBN explicitly. Unlike the relatively well-defined IR frequency ranges

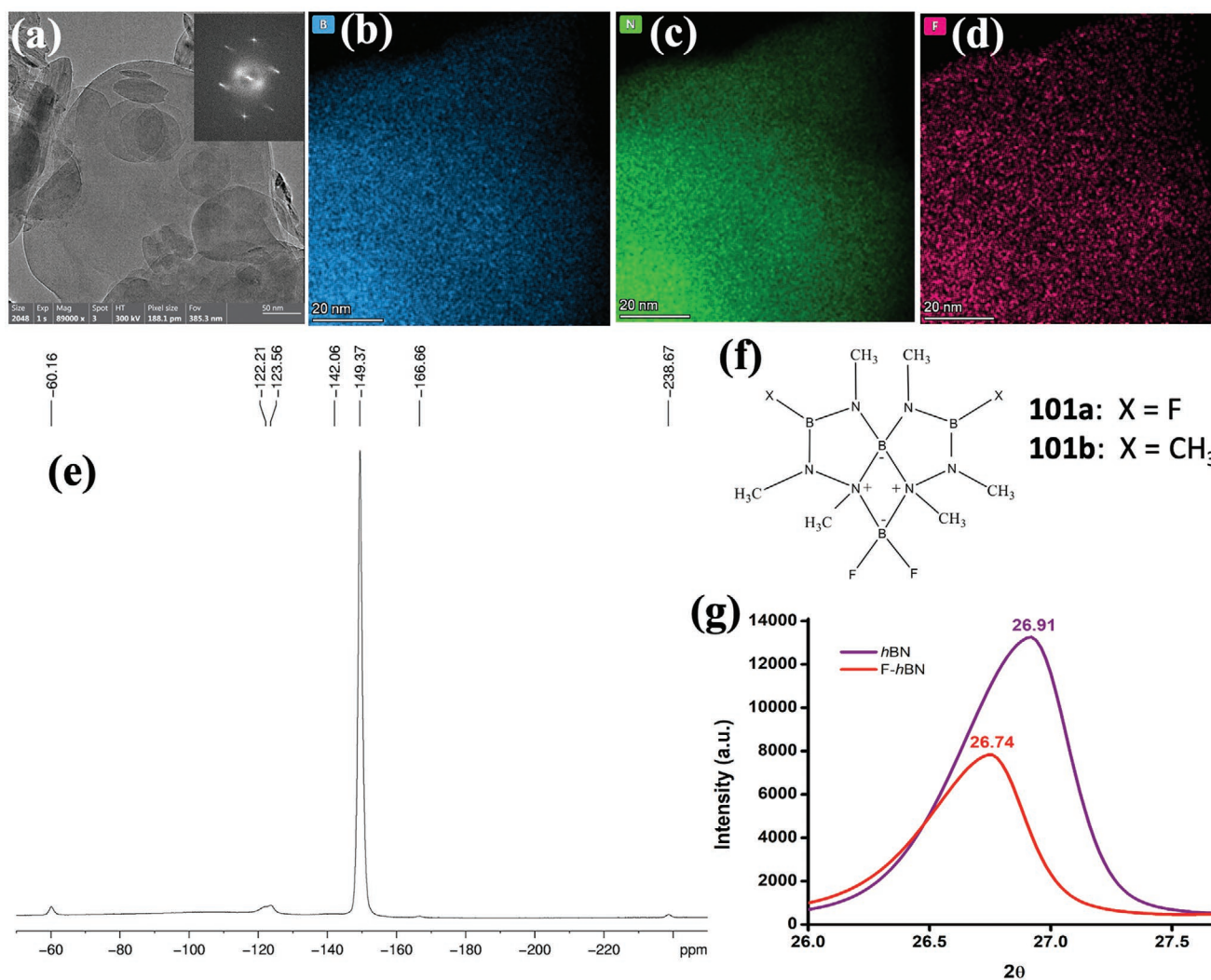


Figure 2. a) STEM studies of fluorinated *h*BN showing the presence of several stacked BN sheets (inset) shows a six-fold SAED symmetry pattern. b–d) Detailed STEM-EDS mapping analysis, which confirms the presence of b) boron, c) nitrogen, and d) fluorine atoms in the fluorinated *h*BN. Additional STEM and EDS results are discussed in the supporting information e) Expanded plot of the 564.6 MHz ^{19}F spectrum of F-*h*BN obtained with 50 kHz MAS (720 scans) and f) The closest models for which ^{19}F chemical shift data have been reported, where 101a exhibits a ^{19}F signal at -157 ppm for the FBN_2 group, while 101a and 101b exhibit a ^{19}F signal at -158 ppm for the F_2BN_2^- group g) shows XRD analysis of pristine *h*BN and *h*BN fluorinated at 50°C for 2h. The fluorinated *h*BN shows a slight shift in the XRD peak, which signifies an increase in the interplanar distance and possibilities of BN sheets exfoliation due to fluorination.

for B-F and N-F vibrations and the relatively well defined XPS binding energies for specific B-F and N-F environments, using MAS ^{19}F NMR to characterize F-*h*BN poses a challenge in that ^{19}F chemical shifts are spread over a very wide frequency range,^[39] and there are no truly suitable model systems with ^{19}F chemical shift data for F-*h*BN.^[11]

The MAS ^{19}F spectra of *h*BN and cubic *c*BN treated with F_2 gas at 50°C are dominated by a strong signal at -149 ppm (Figure 2e and Figure S15, Supporting Information) that we tentatively attribute, as discussed below, to B-F groups in F-*h*BN and F-*c*BN. In the *c*BN-treated sample, the signal at -149 ppm is considerably sharper, and the associated spinning sidebands are weaker. These observations suggest either 1) that the immediate three-dimensional environment on the F giving this signal is considerably more uniform (i.e., smaller chemical

shift anisotropy) in the *c*BN-treated sample or 2) that the more spherical F-*c*BN particles tumble significantly faster than the more disc-like F-*h*BN particles resulting in still greater averaging of the chemical shift anisotropy by MAS and additional line narrowing for the F-*c*BN signals. While *h*BN can, in principle, be functionalized on either side of the layer and give rise to a variety of fluorinated structures, *c*BN, with its diamond-like lattice, can be functionalized only on the periphery.

The broad underlying hump with a maximum near -110 ppm (Figure S15, Supporting Information) is the probe background. Spinning at $\nu_r = 50$ kHz at 564.6 MHz ^{19}F greatly attenuates the spinning sidebands and displaces them at multiples of 89 ppm from the centerband; in addition to the spinning sidebands evident at -238 and -60 ppm ($\pm\nu_r$), extremely weak spinning sidebands (not shown) are evident at -327 and $+29$ ppm ($\pm 2\nu_r$). The

remaining relatively weak signals are centerbands from minor components, which clearly differ in the F-*h*BN and F-cBN samples. The much faster spinning than was possible in our initial study (up to 12 kHz MAS at 376.3 MHz ^{19}F)^[11] enables centerbands to be securely recognized.

The absence of any truly suitable model systems with ^{19}F chemical shift data^[11] severely limits our ability to interpret the strong centerband signal at -149 ppm or the weak centerbands, which might result from species with different fluorination patterns. The structures shown in Figure 2f, with four- and five-membered rings and methyl groups on the periphery, are clearly far from ideal for modeling F-*h*BN but appear to be the closest models for which ^{19}F chemical shift data have been reported. Where 101a exhibits a signal at -157 ppm for the FBN_2 group, while 101a and 101b exhibit a ^{19}F signal at -158 ppm for the F_2BN_2^- group.^[40,41] Since our material gives a signal at -149 ppm, the difference of <10 ppm is inconsequential in light of the very large chemical shift range for ^{19}F ,^[37] especially since the models are far from ideal.

Just based on chemical shift, we cannot rule out BF_4^- (literature chemical shift: -151 ppm).^[39] However, as noted, the signal from F-cBN is significantly sharper than the signal from F-*h*BN (Figure S15, Supporting Information). If these signals resulted from BF_4^- , we would expect essentially the same line-shape in each case, and we would expect F-*h*BN and F-cBN to exhibit a common MAS ^{11}B chemical shift, which they do not. The centerband signals also cannot be from trapped F_2 gas (literature chemical shift: +423 ppm^[39]). Thus, with no other obvious candidates, with the similarity of the ^{19}F chemical shifts in F-*h*BN, F-cBN, the model systems 101a, and 101b, and with XPS and FTIR indicating the dominant presence of B-F functionality, we tentatively attribute the ^{19}F signal at -149 ppm to F-*h*BN. We are not aware of any BN model systems with N-F groups that can serve as even a rough model for fluorinating BN.

The XRD results of *h*BN and F-*h*BN shown in Figure 2g depict their crystalline nature. Another interesting observation was the slight shift in the XRD peak. The pristine BN powders displayed the (002) plane with a 2θ peak around 26.91. In contrast, the F-*h*BN shows a minor shift towards the lower range, exhibiting a 2θ value of ≈ 26.74 , which signifies an increase in the interplanar distance and possibilities for forming free-standing BN sheets. This observation was supported using DFT calculations, demonstrating d-space change from 3.4 Å for pristine *h*BN to 4.6 Å for F-*h*BN.

To understand the thermal stability of the derived B-F and N-F bonds in the synthesized F-*h*BN, we correlated Thermogravimetric analysis (TGA) results with the FTIR and XPS interpretations. We used *h*BN fluorinated at 50 °C for 2 h duration to evaluate the thermal stability of F-*h*BN bonds as that sample exhibited the highest percentage of fluorine content and best resolution of B-F and N-F signals. Figure S16, Supporting Information shows the TGA result of F-*h*BN sample analyzed between 25 and 1000 °C, which shows two significant weight loss events, one at $\approx 40\text{--}80 \pm 5$ °C and another around $210\text{--}270 \pm 5$ °C, which can be assigned to the loss of fluorine atoms bonded to nitrogen (around 3.3 wt%) and boron atoms (≈ 9.2 wt%), respectively (Figure S16, Supporting Information). More details on the B-F and N-F bonds' thermal stability and

their corresponding FTIR and XPS analysis results are discussed in the supporting information (Figures S16–S18, Supporting Information).

We performed theoretical simulations using the universal force field (UFF) and density functional theory (DFT) analyses to elucidate the fluorination process's mechanism and understand the possible kinetics of fluorination (Figure 3a–d). The F-*h*BN displays an increase in interlayer distance of 4.6 Å. due to the effect of fluorination (Figure 3a). *h*BN flakes were passivated with hydrogen (≈ 180 atoms), and we performed the fluorination in the center and at the edges of the BN flakes. The formation of different functionalities was investigated, including B-F, N-F, B-F₂, B-F₃, B-F₄, and N-F₂ groups. Two sets of simulations were performed; in the first, we built different initial configurations for the F atoms in *h*BN, and they were energy minimized using UFF. This forces the system to reach the minimum energy while retaining the fluorine atoms' bonded to the initial specific sites. The use of the UFF method for geometry optimization also favors reduced computational time. After the energy minimizations, we estimated the F atoms' binding energies to determine their feasibility of occurrence. As shown in Figures S19 and S20, Supporting Information we simulated 22 different configurations for F atoms bonded to the *h*BN flake. Of the 22 configurations, four were defective *h*BN flakes, in which we removed one B and one N atom (vacancies) from the center of the flake to examine the fluorination possibility. The binding energies estimated for these 22 configurations are shown in Table S2, Supporting Information.

Among the proposed arrangements, the energetically favorable ones have B-F, B-F₂, N-F, and N-F₂ bonds according to the binding energies. However, due to the presence of dangling bonds, the B-F₂ and N-F₂ groups can only occur at the edges or in the defect sites in *h*BN. From Table S2, Supporting Information, we can infer that B-F₂ ≈ 7.0 eV is more stable than the N-F₂. However, the NF₂ is less stable than the BF and NF groups. This suggests that the B-F, B-F₂, and NF are the most probable groups to form in the majority, which agrees with the experimental observations discussed in Figure 1d–f. Considering the N-F bond, it can occur in an energetically favorable configuration only if there already exists a B-F bond adjacent to it as per structural configurations 9 and 10, shown in Figure 3b. We included the partial electronic charge distribution from the Mulliken population analysis (Figure 3c,d) of an unmodified *h*BN and *h*BN with one F atom bonded to a B atom to understand the fluorination effect further. In Figure 3c, the color scheme varies according to an RGB color scale, in which the electronic charge increases from blue (electron depletion) to red (electron concentration). As seen for unmodified BN, the difference in electronegativity between B and N atoms (B < N) results in N atoms with an excess of negative charge compared to B atoms. Due to this, and considering the boron's sp² hybridization, which results in an empty p_z orbital, the B atoms can attract the F atoms to it. When we add an F bonded to a B, a charge redistribution occurs around the B-F bond resulting in a neighboring N atom with a decreased negative charge (Figure 3d). This scenario may therefore produce an F atom bonding to this N atom.

For the second set of simulations, instead of keeping the specific configuration as before, we performed a complete geometry

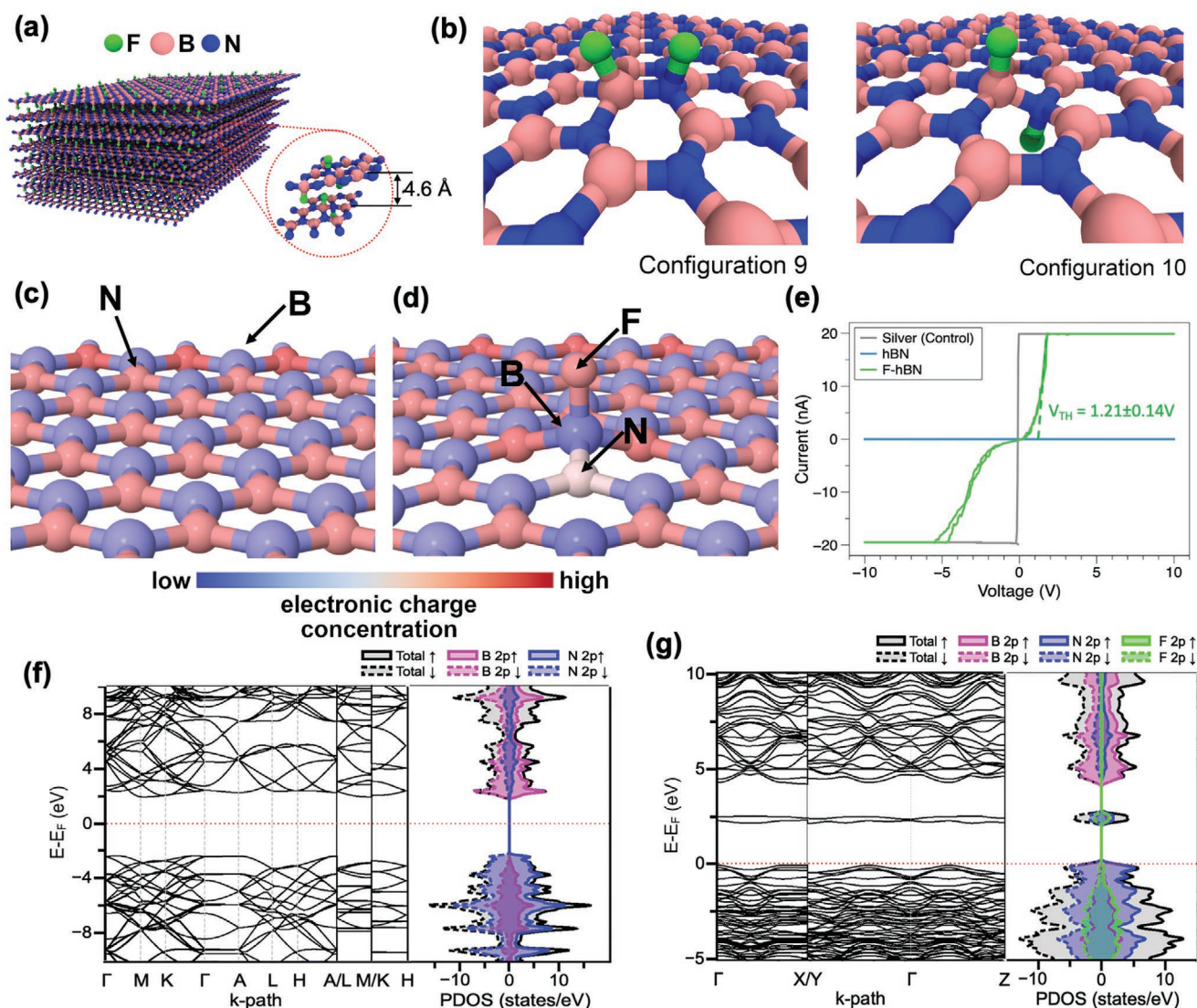


Figure 3. Electronic charge distribution and bandgap of fluorinated hBN. a) 3D view of the fluorinated hBN powders displaying fluorine atoms between the hBN layers. The dotted circle indicates a detailed picture of F-hBN and an increase in interlayer distance of 4.6 Å. due to the effect of fluorination. b) Geometrical structure configurations 9 and 10 tested for F atoms in hBN. The other possible configurations are shown in the Supporting Information (S19 & S20) c) displays partial electronic charge distribution in an unmodified hBN, and d) a single fluorine atom bonded directly to the boron site. The charge scale color at the bottom varies from low electronic charge concentration (blue, electron depletion) to high electronic charge concentration (red, electron concentration). It is possible to see a shift to the red zone due to the addition of fluorine atom and a decreased charge in the blue region in the non-fluorinated hBN sheets. e) IV curve of F-hBN, hBN, and silver paint substrate (control) measured using conductive-AFM microscopy showing semiconducting, insulating, and conducting behavior, respectively. The band structure and projected density of states (PDOS) distribution of f) hBN with a 4.6 eV bandgap and g) F-hBN with a 2.3 eV bandgap, which is a characteristic of a semiconductor behavior. The functionalization of hBN with highly electronegative fluorine creates a doping state inside the bandgap akin to n-doped Si with a raising of the VB towards the Fermi energy.

optimization via DFT using BN flakes with initial B-F₂, B-F₃, and B-F₄ species as shown in configurations 3, 4, and 5 (see Figure S21, Supporting Information). After complete geometry optimization, we can see a preference for these groups and the F atom bonds either to B or N sites, confirming the possibility of having B-F and N-F bonds. The exception occurs for the B-F₃ group, where after the geometry optimization, the B-N bond breaks leading to B-F₂ and an N-F configuration as observed in Figure S21, Supporting Information. Since B-F's bond dissociation energy (732.0 kJ mol⁻¹ at 300 K) is higher than B-N's (377.9 kJ mol⁻¹ at 300 K), this last configuration was found to

be the most favorable.^[42] Overall, our simulation supports the experimental observations suggesting fluorination mechanisms and the formation of both B-F and N-F bonds.

The functionalization of hBN by the fluorine is also reflected in the electronic structure, as seen in the conductive AFM measurements in Figure 3e. To further explore the changes that occurred in the hBN electronic structure due to fluorination, DFT simulations in a projector augmented wave potential (DFT/PAW) were performed for hBN and F-hBN. We initially considered hexagonal supercells of the size of $a = b = 7.5$ Å and $c = 7.7$ Å containing bi-layer systems and 36 (hBN) and 41 (F-hBN)

atoms. Periodic boundary conditions were allowed for all directions with any constraints during the geometry optimizations. The F-*h*BN structure considered contains $\approx 12\%$ of fluorine (5 F atoms per unit cell), in which the F atoms are bonded to B and N, in a configuration similar to the predicted before as the most stable configuration (see Figure 3b). After the geometry optimization, the *h*BN keeps its hexagonal symmetry upon relaxation (P63/mmc space group), and its size changes to $a = b = 7.5 \text{ \AA}$ and $c = 6.8 \text{ \AA}$. However, in a fluorinated case, it is seen that the F atoms distort the *h*BN layer, changing the cell size to $a = b = 7.6 \text{ \AA}$, $c = 8.6 \text{ \AA}$, $\alpha = 110.7^\circ$, $\beta = 78.6^\circ$, and $\gamma = 120.0^\circ$ (P1 space group). In Figures 3f,g, we present the band structure and the projected density of states (PDOS) of *h*BN and F-*h*BN.

From Figure 3f, it can be inferred that the pristine *h*BN may exhibit an indirect bandgap of $\approx 4.6 \text{ eV}$ (from a point within the K- Γ path to M). The PDOS of *h*BN shows that its valence band (VB) has a significant contribution from the N atoms, while for the conduction band (CB), the B atoms contribute the most. This effect is expected since B atoms' hybridization results in an empty p_z orbital, which shares the lone pair's electrons (orbital p_z) of N atoms to create a π bond. As N atoms are more electronegative than B atoms, the electrons of the π system will be more localized on the N atoms, resulting in a significant contribution to the VB formation. Due to this, the almost empty p_z orbital of B will have an essential contribution to the CB. As for F-*h*BN, the addition of highly electronegative fluorine creates a doping state inside the bandgap (See Figure 3g) akin to n-doped Si, which raises the VB towards the Fermi energy. From the band structure, the resulting theoretical bandgap of F-*h*BN decreases to 2.3 eV (50% lower than the *h*BN), characteristic of a semiconductor material (Figure 3g). The bandgap of F-*h*BN is also indirect (from X point to Y point, see Figure 3g). The PDOS indicated that the doping state is created due to the contribution of the F and N atoms. We obtained an underestimated value for the theoretical *h*BN bandgap compared to the experimental observations (of $\approx 6.0 \text{ eV}$).^[43] In general, the bandgap value of *h*BN still remains controversial, and literature supports values ranging from ≈ 3.6 to 7.1 eV , which purely depends on the calculation techniques.^[44–46] This is a well-known and expected effect resulting from the underestimation of the bandgap for bulk materials in theory level used in simulations.^[44,45] However, as we are interested in the qualitative behavior between *h*BN and F-*h*BN, this bandgap underestimation does not affect our analysis and conclusions.

The reduced bandgap and associated transition from insulator to the semiconductor by fluorination can be similarly seen in the experimental *IV* curves by conductive AFM measurements (Figure 3e). The non-functionalized *h*BN is noted to be fully insulating within the range of $\pm 10 \text{ V}$, showing no current flow. Meanwhile, upon fluorination, a semiconducting behavior can be noted for F-*h*BN with a threshold voltage of $1.21 \pm 0.14 \text{ V}$. The control measurement of the silver substrate confirms negligible intrinsic and contact resistance of the system ($\approx 1.3 \mu\Omega$). These observations are in agreement with previous theoretical and experimental studies for F-*h*BN nanosheets.^[21,47]

The frictional properties of *h*BN were first examined due to the similar van der Waals bonding between layers, which provides graphene with its exceptional lubricating ability. It has since been found that *h*BN has similar layer dependence and

bulk frictional properties to other van der Waals materials,^[12] and, as such, it has been synthesized as particles for use as an additive in various lubricant oils.^[13,14] To evaluate the altered friction properties of fluorinated *h*BN particles, the top surface of a random sampling of particles was characterized by friction force microscopy (FFM) using the lateral and normal signals of an atomic force microscope with a diamond-tip cantilever (as schematized in Figure 4a,c). Figure 4b,d, and Figure S22, Supporting Information show the friction and topography maps of pristine and fluorinated *h*BN particles, respectively, and Figure 4e shows the average friction force for normal loads of 0–50 nN.

In the friction maps of Figures 4b,d, it can be noted that the topographies of *h*BN and F-*h*BN particles are non-uniform due to the random slicing of layers at varying thicknesses. The friction is uniform within each sheet area, while increased friction is noted at the edge steps, which is typical of 2D materials due to the Schwoebel-Ehrlich barrier.^[48,49] The particles were wear-free for the range of normal forces of 0–30 nN, while two of six samples for fluorinated *h*BN and one of five for pristine *h*BN showed wear onset in the range of 35–50 nN (Figure S23, Supporting Information). Interestingly, in the F-*h*BN friction map of Figure 4d, high and low friction regions can be detected, corresponding with distinct sheet boundaries across the surface. Comparing this with the topography image (Figure S23, Supporting Information), the regions with higher friction correspond to the surface's lowest height regions. As the sheets in these low-height regions extend beneath the other surface sheets, no edge sites or defects are exposed, which are required for fluorine to intercalate between layers.^[50,51] This likely restricts the bi-lateral fluorination of *h*BN layers resulting in predominantly surface fluorination. The regions with unilateral fluorination present higher friction than the other surface regions but reduced friction compared to pristine *h*BN; across the surface images taken of fluorinated *h*BN, the fully fluorinated low friction regions constitute an estimated 85–90% of surfaces.

Figure 4e shows the average friction force for F-*h*BN and pristine *h*BN surfaces at normal loads from 0–50 nN. Despite pristine *h*BN already offering excellent lubrication abilities, fluorination of *h*BN further reduces the friction force by a factor of 2–3, offering lubricating capabilities amongst the highest performing 2D materials in ambient conditions.^[52] This decrease in friction is also consistent in a pure argon environment suggesting environment-independent behavior (Figure S24, Supporting Information). Surprisingly, despite having a nearly identical lattice structure, this decreased friction is the opposite effect of graphene, which has shown an increase in friction by a factor of 6–7 upon fluorination.^[53,54] Instead, this reduction is similar to the reduced friction effect noted by the fluorination of WS_2 .^[55]

To understand the mechanism for friction improvement of *h*BN caused by fluorination, we further analyzed the structural modifications on *h*BN lattice caused by fluorination using previous simulations executed utilizing DFT/PAW technique. In Figures 4f,g, we displayed the optimized geometry structure of *h*BN and F-*h*BN. DFT simulations in a projector augmented wave potential (DFT/PAW) were performed for *h*BN and F-*h*BN with $\approx 12\%$ fluorination. When an F atom is bonded to a B or N

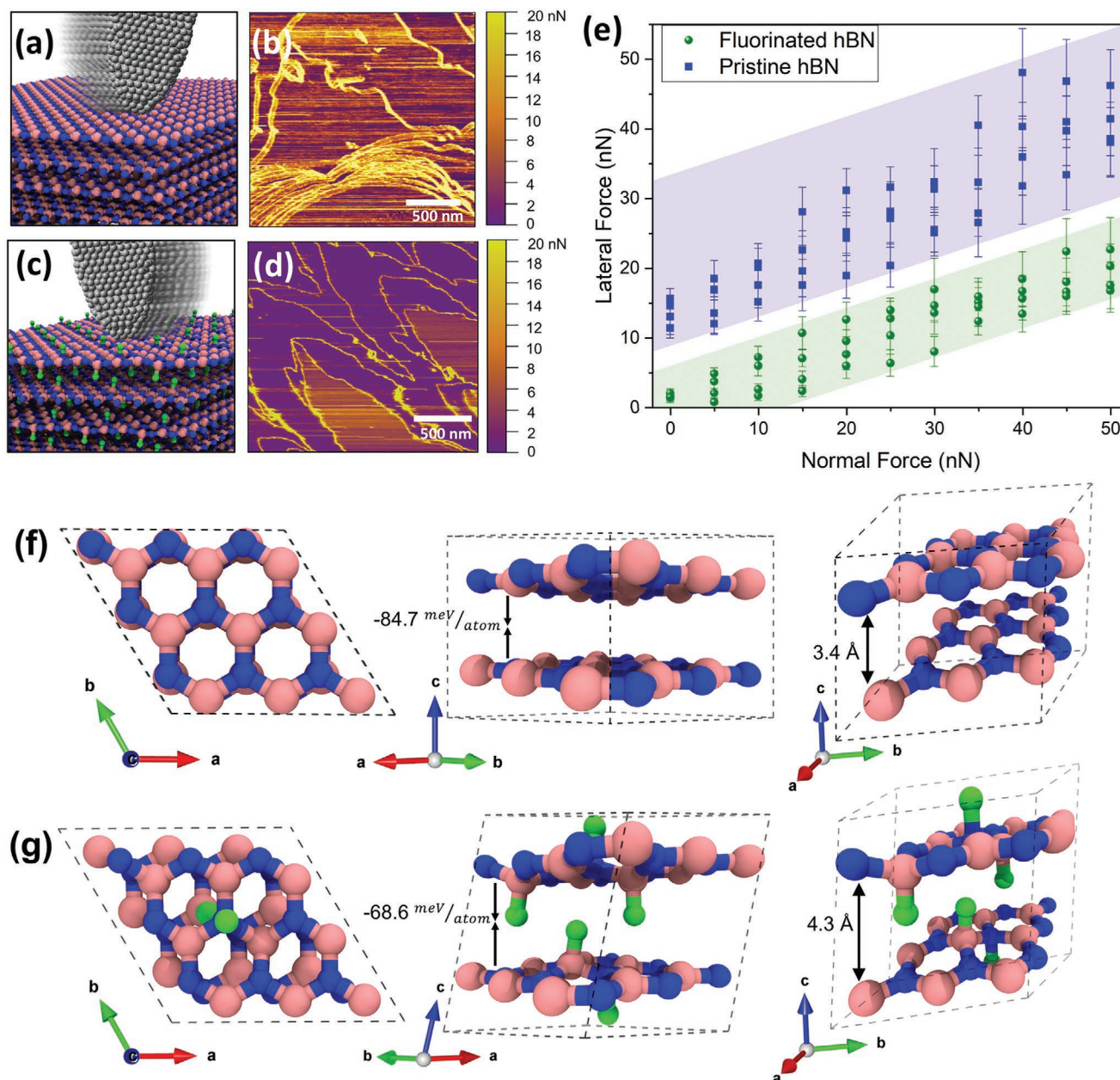


Figure 4. Friction behavior of F-*h*BN and *h*BN samples. Molecular schematic of a diamond AFM tip sliding on a) *h*BN and c) F-*h*BN, b) shows the Friction map of the *h*BN particle surface, and d) displays the friction maps of F-*h*BN particle surface. e) Average friction force for fluorinated and pristine *h*BN surfaces at normal loads from 0–50 nN with standard error. The fluorination of *h*BN reduces the friction force by a factor of 2–3, offering lubricating abilities amongst the highest performing 2D materials in ambient conditions. f) DFT/PAW optimized geometry of *h*BN, the *h*BN keeps its hexagonal symmetry upon relaxation, g) DFT/PAW optimized geometry of fluorinated *h*BN, which shows that the F atoms distort the *h*BN layer, changing the cell size. After the geometry optimization, the *h*BN layers remain at 3.4 Å from each other in the (001) direction. In contrast, for the F-*h*BN layers, the F atoms intercalate between layers exhibiting repulsive forces that force the F-*h*BN layers apart, increasing the (001) distance to 4.6 Å.

atom, there is also a bond length change in the B-N bonds; in the pristine *h*BN, the B-N bonds have a length of 1.45 Å, but in the presence of F atoms, this bond is stretched to 1.51 and 1.52 Å when an F atom is bonded in a B and N, respectively. The resulting B-F and N-F bond length in the F-*h*BN is 1.50 and 1.43 Å, respectively.

After the geometry optimization, the *h*BN layers remain at 3.4 Å from each other in the (001) direction. In contrast, for the

F-*h*BN layers, the F atoms intercalate between layers exhibiting repulsive forces that force the F-*h*BN layers apart, increasing the (001) distance to 4.6 Å. This agrees with XRD measurements (Figure 2g), which suggest increased interplanar distance with fluorination. Furthermore, comparing the interplanar van der Waals energy, *h*BN is calculated to exhibit ≈ -84.7 meV atom⁻¹ while this is reduced to -68.6 meV atom⁻¹ for F-*h*BN. This weakened interplanar potential minimizes the resistance to

interlayer sliding for F-*h*BN, therefore, decreasing the friction force when subjected to shear forces. The change in interlayer spacing is similar to graphene, which has been reported to increase from 3.4 to 6.5–6.7 Å upon fluorination^[56,57] with a similar corresponding decrease in interplanar van der Waals energy.^[58] However, fluorinated graphene also experiences significant out-of-plane buckling of the planar honeycomb structure by >1.4 Å^[59] which disrupts incommensurability and increases the potential energy corrugation leading to friction forces more than six times larger than pure graphene.^[53,54] Meanwhile, for F-*h*BN in the present case, the out-of-plane deformation is calculated only to be 0.4 Å from B-F and 0.15 Å from N-F, thus essentially maintaining the planar uniformity. As a result, the energy landscape for sliding under shear stress remains broadly similar for F-*h*BN compared to *h*BN but with the decreased interlayer interaction potential of F-*h*BN layers, therefore, producing a vastly improved lubricant.

It can be seen that through fluorination of *h*BN particles, several applications become apparent. The bandgap decrease upon fluorination allows the flexibility to derive either insulating or semiconducting properties from a single base material. This creates opportunities for tunable conductivity in single-material systems through local functionalization. Additionally, the friction behavior is significantly improved upon fluorination of *h*BN, which makes F-*h*BN a leading 2D material lubricant. The resulting energy savings of frictional contacts by a further 2–3× compared to standard *h*BN particles, which themselves are already low friction materials, can have broad-reaching impacts in lubricating contacts. These properties can be leveraged for broad applications, and the batch-scale fluorination of *h*BN demonstrated herein exemplifies the feasibility of commercial-scale production.

3. Conclusion

In summary, we developed a straightforward technique to derive fluorinated BN's. This method is considered promising due to its simplicity, chemical/solvent-free approach, and easy scalability. The detailed characterization using several techniques such as XPS, FTIR, TEM, and NMR helped us understand the synthesized fluorinated BN's chemical coordination. This confirmed the possibility of forming both B-F and N-F bonds and the significant variance with changes in fluorination temperature and duration. Interestingly, the formed B-F bonds were found to be stable at temperatures up to ≈200 °C. Our experimental observations were supported by DFT results, which predict several possible scenarios and more stable configurations. More importantly, the bandgap was demonstrated to reduce from 4.6 to 2.3 eV upon fluorination displaying semiconducting behavior as confirmed experimentally. On the other hand, the F-*h*BN displayed an improved friction behavior by a factor of 2–3×, where the primary mechanism was attributed to weaker interlayer interaction caused by electrostatic repulsion of intercalated fluorine atoms between the *h*BN layers. Interestingly, this technique can be extended to fluorinate a wide range of materials, including 2D TMDCs and polymers, which are currently being reviewed. Overall, the addition of new functionality to BN, their semiconducting behavior, and improved

thermal and friction behavior is expected to significantly impact different fields of studies ranging from nanoelectronics to 3D composites and lubricants.

4. Experimental Section

Synthesis of F-*h*BN: *h*BN nanopowders of 70 and 800 nm average particle size were used as received from Momentive and Sigma-Aldrich to synthesize F-*h*BN. The *h*BN powders were placed into a Teflon boat and treated with a constant flow of 10% F₂-90% He gas mixture at either room temperature (RT) or 50 °C for 1 or 2 h, using a custom-built Monel fluorination set up described elsewhere.^[60–62] Caution: Fluorine is a highly toxic, extremely reactive, pale yellow diatomic gas. The experiments are to be carried out with proper care and in a continuous airflow fumehood. The exhausting gas should be connected to a scrubber filled with sodium hydroxide solution to neutralize and collect the residual fluorine.

Characterizations: The fluorinated BN's were analyzed using a Nicolet Fourier transform-infra red (FTIR) spectroscopy. The samples were scanned in the range of 4000–400 cm⁻¹ at an average of 120 scans and with a resolution of 2 cm⁻¹. The obtained spectra were baseline corrected and normalized. The TGA analysis of all the samples was carried out using TA instruments (Q600 simultaneous TGA/DSC). The samples were heated from 25 to 800 °C under the nitrogen atmosphere at a 50 mL min⁻¹ flow rate and a heating rate of 5 °C min⁻¹. We used PHI Quantera XPS with a 5 × 10⁻⁹ Torr chamber pressure and an Al cathode as an X-ray source. The source power was set at 100 W, and pass energies were 26 eV for the core level scans. High-resolution field-emission scanning electron microscopy (HR-SEM) analysis of the F-*h*BN's was carried out using an FEI Quanta 400F ESEM FEG operated at 20 kV. All samples were gold coated (5 nm) before analysis. TEM images including high-resolution TEM and high angle annular dark-field (HAADF), selected area electron diffraction (SAED), electron diffraction spectroscopy (EDS) and elemental mapping, electron energy loss spectroscopy (EELS) measurements were performed with double correctors Titan cubed Themis G2 operated at 300 kV. The microscope is equipped with a Ceta camera, Gatan Quantum 966 energy filter, and an electron monochromator. Before TEM analysis, the F-*h*BN samples were gently sonicated and drop-casted onto holey carbon grids and dried in a vacuum desiccator for three days.

NMR Studies of Fluorinated BN's: F-*h*BN and F-*c*BN were initially studied with a very wide ¹⁹F spectral width (from +817 ppm to -953 ppm) with 40 kHz MAS and 50 kHz MAS (1.3 mm outer diameter rotor) at 564.6 MHz ¹⁹F (dedicated ¹⁹F MAS probe on Bruker 600 MHz spectrometer) to look for any very deshielded or very shielded signals. These preliminary experiments were done with 1.5 μs 54° ¹⁹F pulse, 4.15 ms FID, and 3 s relaxation delay. When no very deshielded or very shielded signals were found, the samples were studied in more detail with a narrower spectral width covering the frequency range with signals. These experiments were done with a 1.5 μs 54° ¹⁹F pulse, 3.02 ms FID, and 3 or 10 s relaxation delay (to verify that relaxation was complete). FIDs were processed without line broadening but with zero-filling from 2 to 16 K for an apparent spectral digital resolution of 0.037 ppm. A ¹⁹F background spectrum was acquired with a rotor of glycine spinning at 50 kHz. Chemical shifts are relative to the CF₃ group in flufenamic acid {N-[3-(trifluoromethyl)phenyl]anthranilic} defined as -61.5 ppm.^[63]

Theoretical Studies: The theoretical simulations of finite systems were performed using molecular mechanics (MM) using the universal force field (UFF)^[64] and density functional theory (DFT), with a 6–31G(d) basis set functions and the Becke three-parameter Lee-Yang-Parr exchange-correlation functional (B3LYP).^[65,66] The binding energies (*E_b*) were evaluated considering the following equation: $E_b = E_{hBN+nF} - (E_{hBN} + E_{nF})$, in which *n* is the number of F atoms bonded to BN and *E_{hBN+nF}*, *E_{hBN}*, and *E_{nF}*, respectively, the total energy for a fluorinated BN, unmodified BN, and the F atoms. As for crystalline systems, DFT simulations were performed with a projector augmented wave potential (PAW) in

a generalized gradient approximation (GGA) with the Perdew, Burke, and Ernzerhof (PBE) exchange-correlation functional. A Monkhorst-Pack k -mesh of $4 \times 4 \times 4$ was used to sample the Brillouin zone, and the Kohn–Sham orbitals were expanded in a plane-wave basis set with a kinetic energy cutoff of 50 Ry (≈ 680 eV). All theoretical simulations were performed using Avogadro^[67] and GAUSSIAN09,^[68] and QUANTUM ESPRESSO^[58] softwares.

Friction Force Measurements: Friction force microscopy (FFM) was carried out using an Asylum MFP 3D atomic force microscope (AFM) on pristine and functionalized hBN samples under ambient conditions at a scan speed of $0.8 \mu\text{m s}^{-1}$. Sharp diamond tip AFM cantilevers (K-Tek Nanotechnology) were used to perform FFM, where the normal and lateral stiffnesses were calibrated using Sader's method.^[69,70] The cantilever had standard stiffness of $\approx 0.07 \text{ N m}^{-1}$ and a torsional constant of $\approx 8.8 \times 10^{-9} \text{ N m}$. The average sensitivity was calibrated against the silicon wafer, and the lateral sensitivity of 86 nm V^{-1} was measured against a cleaved KBr block.^[70] Friction was measured via FFM as a function of increasing the average load from 0 to 50 nN. Each cantilever was used to measure alternating particle types to ensure any tip wear or contact changes were accounted for consistently in both samples. The hBN particles were spread across carbon tape during testing to restrict rolling or movement while FFM was applied to the surface.

Conductivity Measurements: The IV characteristics of F-hBN, hBN, and the silver substrate (control) were determined by conductive AFM measurements using the ORCA module of an Asylum Cypher atomic force microscope. Conductive AFM probes of pure PtIr (12PtIr400B, $k = 0.6 \text{ N m}^{-1}$) from Rocky Mountain Nanotechnology (Utah, USA) were used to measure the system's current flow. The silver paste was deposited on a gold substrate, and conductivity measurements were used to determine the system's negligible contact resistance without hBN.

Supporting Information

Supporting Information is available from the Wiley Online Library or from the author.

Acknowledgements

The authors thank Baker Hughes Company for sponsoring this work under Agreement No. 6-57933. The authors also acknowledge the Electron Microscopy Center (EMC), Rice University, for their support in the analysis of samples. The ^{19}F MAS NMR experiments were carried out at the National High Magnetic Field Lab (NHMFL) supported by the NSF Cooperative agreement DMR-1644779 and the State of Florida. EFO and DSG would like to thank the Brazilian agencies CNPq and FAPESP (Grants 2016/18499-0, and 2019/07157-9) for financial support. Computational support from the Center for Computational Engineering and Sciences at Unicamp through the FAPESP/CEPID Grant No. 2013/08293-7 and the Center for Scientific Computing (NCC/GridUNESP) of São Paulo State University (UNESP) is also acknowledged.

Conflict of Interest

The authors declare no conflict of interest.

Author Contributions

A.K.M. conceived and designed the work, coordinated in all experiments and analysis. V.N.K. fluorinated the BN samples. D.S. performed XPS and analyzed the results. P.S. T.A., and T.F. carried out IV studies and friction measurements. E.F.O. and D.S.G. simulated the theoretical

modeling. L.B.A. and R.F. performed detailed NMR studies. G.G. carried out HRTEM analysis, and R.V. V.S. helped in the interpretation of data and experiments. A.K.M. and P.M.A. supervised the project and experiments. All authors discussed the results and contributed to the writing and editing of the manuscript.

Data Availability Statement

Research data are not shared.

Keywords

2D materials, bandgap, friction, functionalization, semiconducting

Received: August 5, 2021

Revised: September 27, 2021

Published online:

- [1] S. S. Chou, M. De, J. Kim, S. Byun, C. Dykstra, J. Yu, J. Huang, V. P. Dravid, *J. Am. Chem. Soc.* **2013**, *135*, 4584.
- [2] X. S. Chu, A. Yousaf, D. O. Li, A. A. Tang, A. Debnath, D. Ma, A. A. Green, E. J. G. Santos, Q. H. Wang, *Chem. Mater.* **2018**, *30*, 2112.
- [3] L. Niu, K. Li, H. Zhen, Y.-S. Chui, W. Zhang, F. Yan, Z. Zheng, *Small* **2014**, *10*, 4651.
- [4] C. Tang, Y. Bando, Y. Huang, S. Yue, C. Gu, F. Xu, D. Golberg, *J. Am. Chem. Soc.* **2005**, *127*, 6552.
- [5] D. Voiry, A. Goswami, R. Kappera, C. d. C. E. Silva, D. Kaplan, T. Fujita, M. Chen, T. Asefa, M. Chhowalla, *Nat. Chem.* **2015**, *7*, 45.
- [6] X. Chen, A. R. McDonald, *Adv. Mater.* **2016**, *28*, 5738.
- [7] C. R. Dean, A. F. Young, I. Meric, C. Lee, L. Wang, S. Sorgenfrei, K. Watanabe, T. Taniguchi, P. Kim, K. L. Shepard, J. Hone, *Nat. Nanotechnol.* **2010**, *5*, 722.
- [8] W. Ouyang, D. Mandelli, M. Urbakh, O. Hod, *Nano Lett.* **2018**, *18*, 6009.
- [9] M. Noor-A-Alam, H. J. Kim, Y.-H. Shin, *Phys. Chem. Chem. Phys.* **2014**, *16*, 6575.
- [10] A. Bhattacharya, S. Bhattacharya, G. P. Das, *Phys. Rev. B – Condens. Matter Mater. Phys.* **2012**, *85*, 035415.
- [11] S. Radhakrishnan, D. Das, A. Samanta, C. A. De Los Reyes, L. Deng, L. B. Alemany, T. K. Weldeghiorghis, V. N. Khabashesku, V. Kochat, Z. Jin, P. M. Sudeep, A. A. Martí, C.-W. Chu, A. Roy, C. S. Tiwary, A. K. Singh, P. M. Ajayan, *Sci. Adv.* **2017**, *3*, e1700842.
- [12] C. Lee, Q. Li, W. Kalb, X. Z. Liu, H. Berger, R. W. Carpick, J. Hone, *Science (80-)*. **2010**, *328*, 76.
- [13] C. J. Reeves, P. L. Menezes, M. R. Lovell, T.-C. Jen, *Tribol. Lett.* **2013**, *51*, 437.
- [14] O. N. Çelik, N. Ay, Y. Göncü, *Part. Sci. Technol.* **2013**, *31*, 501.
- [15] A. Falin, Q. Cai, E. J. G. Santos, D. Scullion, D. Qian, R. Zhang, Z. Yang, S. Huang, K. Watanabe, T. Taniguchi, M. R. Barnett, Y. Chen, R. S. Ruoff, L. H. Li, *Nat. Commun.* **2017**, *8*, 15815.
- [16] T. Sainsbury, A. Satti, P. May, Z. Wang, I. McGovern, Y. K. Gun'ko, J. Coleman, *J. Am. Chem. Soc.* **2012**, *134*, 18758.
- [17] A. Pakdel, Y. Bando, D. Golberg, *ACS Nano* **2014**, *8*, 10631.
- [18] X. Li, X. Hao, M. Zhao, Y. Wu, J. Yang, Y. Tian, G. Qian, *Adv. Mater.* **2013**, *25*, 2200.
- [19] F. Xiao, S. Naficy, G. Casillas, M. H. Khan, T. Katkus, L. Jiang, H. Liu, H. Li, Z. Huang, *Adv. Mater.* **2015**, *27*, 7196.
- [20] W. Lei, V. N. Mochalin, D. Liu, S. i. Qin, Y. Gogotsi, Y. Chen, *Nat. Commun.* **2015**, <https://doi.org/10.1038/ncomms9849>.

- [21] Y. Liao, Z. Chen, J. W. Connell, C. C. Fay, C. Park, J.-W. Kim, Y. Lin, *Adv. Funct. Mater.* **2014**, *24*, 4497.
- [22] C. Chen, J. Wang, D. Liu, C. Yang, Y. Liu, R. S. Ruoff, W. Lei, *Nat. Commun.* **2018**, <https://doi.org/10.1038/s41467-018-04294-6>.
- [23] T. Sainsbury, A. O'Neill, M. K. Passarelli, M. Seraffon, D. Gohil, S. Gnaniyah, S. J. Spencer, A. Rae, J. N. Coleman, *Chem. Mater.* **2014**, *26*, 7039.
- [24] C. Zhi, Y. Bando, C. Tang, S. Honda, K. Sato, H. Kuwahara, D. Golberg, *Angew. Chemie – Int. Ed.* **2005**, *44*, 7932.
- [25] Q. Weng, X. Wang, X. Wang, Y. Bando, D. Golberg, *Chem. Soc. Rev.* **2016**, 3989, <https://doi.org/10.1039/c5cs00869g>.
- [26] Z. Zhou, J. Zhao, Z. Chen, P. V. R. Schleyer, *J. Phys. Chem. B* **2006**, *110*, 25678.
- [27] J. Zeng, K.e-Q. Chen, C. Q. Sun, *Phys. Chem. Chem. Phys.* **2012**, *8032*, <https://doi.org/10.1039/c2cp23937j>.
- [28] M. Du, X. Li, A. Wang, Y. Wu, X. Hao, M. Zhao, *Angew. Chemie – Int. Ed.* **2014**, *53*, 3645.
- [29] Q. Weng, D. G. Kvashnin, X. Wang, O. Cretu, Y. Yang, M. Zhou, C. Zhang, D.-M. Tang, P. B. Sorokin, Y. Bando, D. Golberg, *Adv. Mater.* **2017**, *29*, 1700695.
- [30] Y. Yang, Y. Liu, Y. Li, M. Gao, H. Pan, *J. Mater. Chem. A* **2015**, *3*, 570.
- [31] M. A. A. Beg, H. C. Clark, *Can. J. Chem.* **1962**.
- [32] H. J. Emeléus, J. M. Shreeve, R. D. Verma, *Adv. Inorg. Chem.* **1989**, [https://doi.org/10.1016/S0898-8838\(08\)60195-6](https://doi.org/10.1016/S0898-8838(08)60195-6).
- [33] K. O. Schack, C. J. Christie, *Inorg. Chem.* **1978**, *17*, 2749.
- [34] A. M. Qureshi, F. Aubke, *Can. J. Chem.* **1970**, *48*, 3117.
- [35] L. Ci, L. Song, C. Jin, D. Jariwala, D. Wu, Y. Li, A. Srivastava, Z. F. Wang, K. Storr, L. Balicas, F. Liu, P. M. Ajayan, *Nat. Mater.* **2010**, *9*, 430.
- [36] Z. Liu, L. Ma, G. Shi, W. Zhou, Y. Gong, S. Lei, X. Yang, J. Zhang, J. Yu, K. P. Hackenberg, A. Babakhani, J.-C. Idrobo, R. Vajtai, J. Lou, P. M. Ajayan, *Nat. Nanotechnol.* **2013**, *8*, 119.
- [37] A. Ul Ahmad, H. Liang, Q. Abbas, S. Ali, M. Iqbal, A. Farid, A. Abbas, Z. Farooq, *Ceram. Int.* **2019**, *45*, 19173.
- [38] Y. Bai, J. Zhang, Y. Wang, Z. Cao, L. An, B. Zhang, Y. Yu, J. Zhang, C. Wang, *ACS Appl. Nano Mater.* **2019**, *2*, 3187.
- [39] S. Berger, S. Braun, H. O. Kalinowski, *NMR Spectroscopy of the Non-metallic Elements*, Wiley, Chichester **1997**, p. 1–1098.
- [40] V. Wray, *Annu. Reports NMR Spectrosc.* **1980**, *10B*, 1.
- [41] H. Fußstetter, H. Nöth, W. Winterstein, *Chem. Ber.* **1977**, *110*, 1931.
- [42] Y. R. Luo, *Handbook of Bond Dissociation Energies in Organic Compounds*, CRC Press, Boca Raton **2002**, <https://doi.org/10.1201/9781420039863>.
- [43] G. Cassabois, P. Valvin, B. Gil, *Nat. Photonics* **2016**, *10*, 262.
- [44] L. Liu, Y. P. Feng, Z. X. Shen, *Phys. Rev. B* **2003**, *68*, 104102.
- [45] Y. Malozovsky, C. Bamba, A. Stewart, L. Franklin, D. Bagayoko, *J. Mod. Phys.* **2020**, 928, <https://doi.org/10.4236/jmp.2020.116057>.
- [46] S. Roy, et al., *Adv. Mater.* n/a, 2101589.
- [47] Y. Xue, Q. Liu, G. He, K. Xu, L. Jiang, X. Hu, J. Hu, *Nanoscale Res. Lett.* **2013**, *8*, 49.
- [48] P. Egberts, Z. Ye, X. Z. Liu, Y. Dong, A. Martini, R. W. Carpick, *Phys. Rev. B – Condens. Matter Mater. Phys.* **2013**, *88*, 035409.
- [49] T. Arif, S. Yadav, G. Colas, C. V. Singh, T. Filleter, *Adv. Mater. Interfaces* **2019**, *6*, 1901246.
- [50] J. T. Robinson, J. S. Burgess, C. E. Junkermeier, S. C. Badescu, T. L. Reinecke, F. K. Perkins, M. K. Zalalutdniov, J. W. Baldwin, J. C. Culbertson, P. E. Sheehan, E. S. Snow, *Nano Lett.* **2010**, *10*, 3001.
- [51] K. I. Ho, C. H. Huang, J. H. Liao, W. Zhang, L. J. Li, C. S. Lai, C. Y. Su, et al., *Sci. Rep.* **2014**, *4*, 5893.
- [52] D. Berman, A. Erdemir, A. V. Sumant, *Mater. Today* **2014**, *17*, 31.
- [53] S. Kwon, J.-H. Ko, K.-J. Jeon, Y.-H. Kim, J. Y. Park, *Nano Lett.* **2012**, *12*, 6043.
- [54] Q. Li, X.-Z. Liu, S.-P. Kim, V. B. Shenoy, P. E. Sheehan, J. T. Robinson, R. W. Carpick, *Nano Lett.* **2014**, *14*, 5212.
- [55] S. Radhakrishnan, D. Das, L. Deng, P. M. Sudeep, G. Colas, C. A. Los Reyes, S. Yazdi, C. W. u Chu, A. A. Martí, C. S. Tiwary, T. Filleter, A. K. Singh, P. M. Ajayan, *Adv. Mater.* **2018**, *30*, 1803366.
- [56] Y. Liu, J. Li, S. Yi, X. Ge, X. Chen, J. Luo, *Carbon N. Y.* **2020**, *167*, 122.
- [57] Z. Wang, J. Wang, Z. Li, P. Gong, J. Ren, H. Wang, X. Han, S. Yang, *RSC Adv.* **2012**, *2*, 11681.
- [58] L.-F. Wang, T.-B. Ma, Y.-Z. Hu, H. Wang, T.-M. Shao, *J. Phys. Chem. C* **2013**, *117*, 12520.
- [59] H. Āzahin, M. Topsakal, S. Ciraci, *Phys. Rev. B – Condens. Matter Mater. Phys.* **2011**, *83*, 115432.
- [60] Y. u Liu, Z. Gu, J. L. Margrave, V. N. Khabashesku, *Chem. Mater.* **2004**, 3924.
- [61] V. N. Khabashesku, W. E. Billups, J. L. Margrave, *Acc. Chem. Res.* **2002**, *35*, 1087.
- [62] V. N. Khabashesku, M. AshokKumar, P. M. Ajayan, United States Patent Application Pub.No.: US2021/018637A1, **2021**
- [63] R. Fu, A. J. Hernández-Maldonado, *J. Magn. Reson.* **2018**, *293*, 34.
- [64] A. K. Rappe, C. J. Casewit, K. S. Colwell, W. A. Goddard, W. M. Skiff, *J. Am. Chem. Soc.* **1992**, *114*, 10024.
- [65] A. D. Becke, *J. Chem. Phys.* **1993**, *98*, 1372.
- [66] P. J. Stephens, F. J. Devlin, C. F. Chabalowski, M. J. Frisch, *J. Phys. Chem.* **1994**, *98*, 11623.
- [67] M. D. Hanwell, D. E. Curtis, D. C. Lonie, T. Vandermeersch, E. Zurek, G. R. Hutchison, *J. Cheminform.* **2012**, <https://doi.org/10.1186/1758-2946-4-17>.
- [68] M. J. Frisch et al. Gaussian09 Revision D.01, Gaussian Inc. Wallingford CT. Gaussian 09 Revision C.01 2010.
- [69] J. E. Sader, J. W. M. Chon, P. Mulvaney, *Rev. Sci. Instrum.* **1999**, *70*, 3967.
- [70] R. J. Cannara, M. Eglin, R. W. Carpick, *Rev. Sci. Instrum.* **2006**, *77*, 053701.